Development of a Fe–Cr alloy for interconnect application in intermediate temperature solid oxide fuel cells

Bin Hua [a], Jian Pu [a,*], Fengshuang Lu [b], Jianfu Zhang [b], Bo Chi [a], Li Jian [a]

[a] School of Materials Science and Engineering, State Key Laboratory of Materials Processing and Die & Mould Technology, Huazhong University of Science & Technology, Wuhan, Hubei 430074, PR China
[b] China Iron & Steel Research Institute Group, Beijing 10081, PR China

ARTICLE INFO

ABSTRACT

The oxidation behavior and electrical property of a newly designed Fe–Cr alloy with addition of 1.05 wt.% Mn, 0.52 wt.% Ti, 2.09 wt.% Mo and other elements, such as La, Y and Zr have been investigated isothermally or cyclically at 750 °C in air for up to 1000 h. With a coefficient of thermal expansion matched to SOFC cell components, the alloy demonstrates excellent oxidation resistance and low area specific resistance of the oxide scale. The thermally grown oxide scale presents a multi-layered structure with conductive Mn–Cr spinel in-between the underneath Cr_2O_3 and the top Mn_2O_3. The oxidation rate constants obtained under both isothermal and cyclic oxidation condition are in the range of 5.1×10^{-14} to 7.6×10^{-14} g^2 cm^{-4} s^{-1}, and the measured area specific resistance at 750 °C after 1000 h oxidation is around 10 mΩ cm^2, lower than that of the conventional Fe–Cr stainless steels and comparable with that of the Ni-based alloys. Thermal cycling seems to improve the oxide scale adherence and promotes the formation of the highly conductive Mn_2O_3, and in turn, to enhance the oxidation resistance and electrical property.

© 2009 Elsevier B.V. All rights reserved.

1. Introduction

The interconnect is a critical component in the stack of solid oxide fuel cells (SOFCs), which provides electrical connection between adjacent cells, physically separates the oxidant and fuel gases and distributes the gases to electrodes. In the last decade, significant progress has been made to reduce the operating temperature of SOFCs from near 1000 °C to an intermediate temperature range of about 600–800 °C by either reducing the thickness of conventional electrolyte or using improved electrolyte and electrodes. Reduced operating temperature allows the use of metallic alloys for the interconnect application, offering significant advantages in electric and thermal conductivities, mechanical integrity, fabrication and cost. Among all metallic materials, Cr_2O_3-forming alloys are the most favorable candidates which forms Cr_2O_3 in the scale with low growth rate and high electric conductivity in the intermediate temperature range, compared to the insulating Al_2O_3 and SiO_2-forming counterparts [1,2]. Thus, Fe–Cr ferritic stainless steels, with a coefficient of thermal expansion (CTE) closely matched to that of the cell components, have been intensively investigated [3–7].

Nevertheless, as interconnect materials in the intermediate temperature range, the Cr_2O_3-forming ferritic stainless steels are still facing challenges in the aspects of cathode Cr-poisoning, insufficient oxidation resistance and electrical conductivity for long-term applications. Cr vaporization primarily in the form of CrO_3 and $CrO_2(OH)_2$ resulted from Cr-containing oxides, especially Cr_2O_3, is an unsolved issue of the Cr_2O_3-forming ferritic stainless steels for applications in SOFC cathode environment. In the presence of water vapor, the volatile Cr species preferably formed and subsequentially deposited on the surface of the cathode and/or at the cathode/electrolyte interface, leading to significant reductions in cathode activity and cell performance [8–10]. The thermally grown oxide scales of the ferritic stainless steels may overgrow to as thick as tens of micrometers during SOFC's lifetime, resulting in high electrical resistance and even scale spallation due to the thermal stresses induced by thermal expansion mismatch between the scale and substrate. All of these will cause unacceptable degradation in SOFC stack performance [11,12].

It is preferred that the interconnect alloys must exhibit a long-term stability in SOFC environments with oxygen partial pressure varying from 0.21 atm (in air) to 10^{-18} to 10^{-8} atm (in fuel gas). For commercial ferritic stainless steels, surface modifications, such as applying protective coatings, are likely required with additional cost to promote the oxidation resistance, depress the Cr volatilization, and improve the scale conductivity and adherence [13–16]. An alternative approach is to develop new alloys for the interconnects by modifying the composition of the conventional Fe–Cr stainless steels. The presence of Mn in Fe–Cr alloys can form double-layered oxide scale with $(Mn,Cr)_3O_4$ on top of Cr_2O_3, which improves the

Table 1
Chemical composition of the developed Fe–Cr alloy (wt.%).

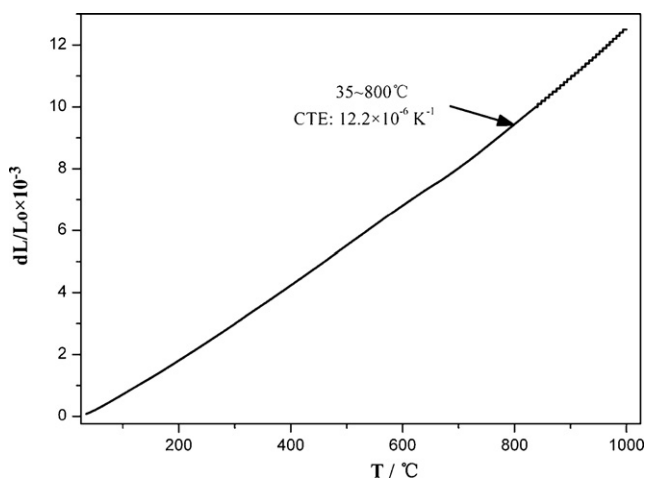| Element	Cr	Mn	Ti	La	Y	Zr	Mo	C	S	P	Si	Fe
Fe–Cr alloy	16.56	1.05	0.52	0.005	0.018	0.11	2.09	0.002	< 0.001	0.0094	0.038	Bal.

electrical conductivity of the scale and suppresses the Cr evaporation due to $(Mn,Cr)_3O_4$ possesses higher electrical conductivity and lower Cr evaporation pressure than that of Cr_2O_3, even though Cr evaporation from $(Mn,Cr)_3O_4$ spinel is still unavoidable, especially during the early stage of the oxidation [17–19]. The addition of Ti in the alloy would be expected to enhance the electrical conductivity of the oxide scale by forming Ti doped Cr_2O_3 or more conductive TiO_2 [20–22]. Elements, such as Y, La and Zr, in the alloy are also known for promoting oxidation resistance, scale adherence and conductivity [16].

To develop a new alloy that can fulfill the requirements of SOFC interconnect on metallic alloys by forming a protective, conductive and less Cr–volatile oxide scale in SOFC operating atmospheres, a low carbon content Fe–Cr-based alloy with addition of Mn, Ti, Mo, Zr, La and Y was presented. This alloy was subjected to long-term isothermal and cyclic oxidation in air at 750 °C, respectively. The phase, microstructure, composition and electrical property of the thermally grown oxide scale were characterized and evaluated accordingly.

2. Experimental

The Fe–Cr-based alloy was prepared with high-purity elemental materials by arc melting in vacuum and hot rolled to 1 mm thick sheet, followed by conventional heat treatment. The chemical composition of the alloy was analyzed as listed in Table 1. It has a coefficient of thermal expansion (CTE) of $12.2 \times 10^{-6}\,K^{-1}$ in the temperature range between 35 and 800 °C as shown in Fig. 1, which is well matched to that of SOFC cell components (typically in the range of $10–13 \times 10^{-6}\,K^{-1}$).

Rectangular coupons for oxidation evaluation with a dimension of 25 mm × 25 mm × 1 mm were cut from the sheet by using an electrical discharge machine. Prior to oxidation, the coupon surfaces were mechanically polished with sandpapers up to 1200 grit and then ultrasonically cleaned in acetone and ethanol, respectively. Isothermal oxidation was performed at 750 °C in ambient air for up to 1000 h. The weight of all the coupons before and after oxidation was measured for calculating the weight gain upon oxidation. In order to understand the effect of thermal cycling on the oxidation behavior, cyclic oxidation was also conducted at 750 °C in air. 14 cycles between room temperature and 750 °C were performed within 1000 h oxidation. The weight gain after each thermal cycle was recorded. All the weight measurements were carried out by using a Sartorius BT-25S electronic balance with an accuracy of 10^{-5} g. The oxidation kinetics was obtained by plotting the weight gain against oxidation time.

The phase structure of the thermally grown oxide scale was identified using a PANalytical X'Pert PRO X-ray diffractometer (XRD) with CuKα radiation under the conditions of 40 kV and 40 mA. The scanning rate was 15° min⁻¹ and the scanning angle 2θ ranged from 20° to 80°. The microstructure and composition of the oxide scale were characterized by scanning electron microscopy (SEM, FEI QUANTA 200) with energy dispersive spectroscopy (EDS) attachment. The coefficient of thermal expansion was measured by a NETZSCH thermal dilatometer DIL-402C.

The electrical property of the oxidized samples was evaluated using the four-probe dc technique at temperatures in between 400 and 800 °C in air. The two main surfaces of the oxidized coupon were printed with Ag paste onto which Ag mesh with two spark welded Ag leads was compressed for applying electrical current and reading the voltage drop. The experimental assembly is schematically shown in Fig. 2. A constant current I of 200 mA was applied from a direct current power source (ITECH, IT6270) across any two Ag leads attached to the opposite surfaces, and the voltage drop V across the thickness of the oxidized specimen was measured with another two Ag leads using a voltage meter (LEEF, ZYB-1). The area specific resistance (ASR) of the oxidized coupon, which reflects both the electrical conductivity and thickness of the oxide scale, was calculated according to

$$ASR = \left(\frac{1}{2}\right) RS \tag{1}$$

where R is the electrical resistance calculated by the Ohm's law, $R = V/I$, S is the area covered by the Ag paste, and the factor of 1/2 is for the consideration that R is contributed by the oxide scales on the two main surfaces.

3. Results and discussion

3.1. Phase structure and morphology of the oxide scale

Fig. 3 shows the XRD patterns of the Fe–Cr alloy oxidized isothermally and cyclically at 750 °C in air for up to 1000 h. Comparing the diffraction peaks generated from the oxidized samples with the JCPDS files, it can be seen that the predominate phases in the oxide scales are Mn–Cr spinel, Cr_2O_3 and Mn_2O_3. Moreover, weak diffraction peaks showing the existence of TiO_2 are also detected, confirming the formation of TiO_2 during the oxidation. The diffraction peak positions of Mn_2O_3 and TiO_2 match those of JCPDS files

Fig. 1. Thermal expansion behavior of the developed Fe–Cr alloy.
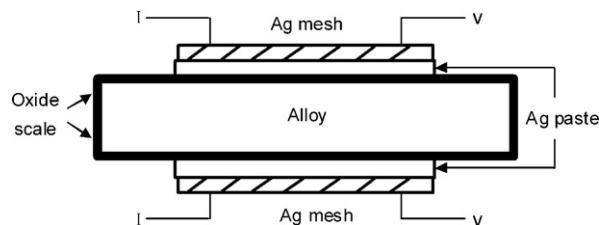
Fig. 2. Schematic diagram for the measurement of area specific resistance (ASR).
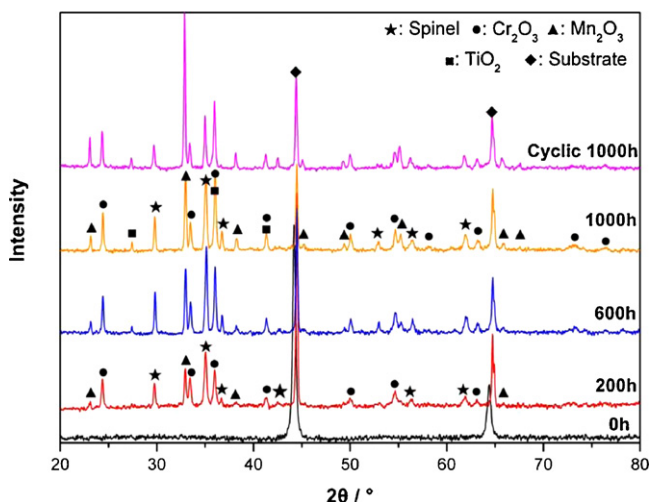
Fig. 3. XRD patterns of the Fe–Cr alloy oxidized at 750 °C in air for different times.

#89-4836 and #89-4202 very well, respectively; and the detected spinel seems to match Mn–Cr spinel with a composition close to $Mn_{1.5}Cr_{1.5}O_4$. However, slight shift of diffraction peaks to the lower angle from those in JCPDS files #84-1616 (Cr_2O_3) and #33-0892 ($Mn_{1.5}Cr_{1.5}O_4$) can be observed. This phenomenon may suggest that the thermally grown Cr_2O_3 and Mn–Cr spinel do not have the stoichiometric compositions of Cr_2O_3 and $Mn_{1.5}Cr_{1.5}O_4$; and Mn may exist in Cr_2O_3 and the detected spinel may have higher Mn content than that in $Mn_{1.5}Cr_{1.5}O_4$ which expand the lattice parameters and shift the diffraction peak positions [23]. As isothermal oxidation time prolonged, the diffraction from the Mn–Cr spinel, Cr_2O_3, Mn_2O_3 and TiO_2 became more intense, implying that the oxide scale grew thicker. In contrary, the diffraction intensity of the alloy substrate decreased gradually and the peak positions shifted increasingly to the higher angle. This phenomenon implies that the oxidation is basically controlled by the outward diffusion of cations from the alloy substrate, resulting in depletion of alloying elements and shrinking lattice parameters in the substrate near the oxide scale. Comparing the diffraction patterns from the specimens oxidized isothermally and cyclically at 750 °C in air for 1000 h, the diffraction intensity of Mn_2O_3 formed upon the cyclic oxidation is observably higher than that formed during the isothermal oxidation. This suggests a faster outward diffusion of Mn during cyclic oxidation.

Fig. 4 shows the SEM secondary electron images of the surface oxide isothermally formed at 750 °C in air. No scale spallation was observed on any of the oxidized specimens. After 200 h oxidation, as shown in Fig. 4a and b, the surface is rather uniform and all the surface is covered by prism-like grains and compact clusters (location C in Fig. 4b). The EDS results from the prism-like grain and the cluster are shown in Table 2. The atomic ratio of Cr to Mn is approximately 1:1 for the prism-like grains (locations A and B in Fig. 4b), indicating that the prism-like grains are Mn–Cr spinel with a composition close to that of $Mn_{1.5}Cr_{1.5}O_4$. And the oxide
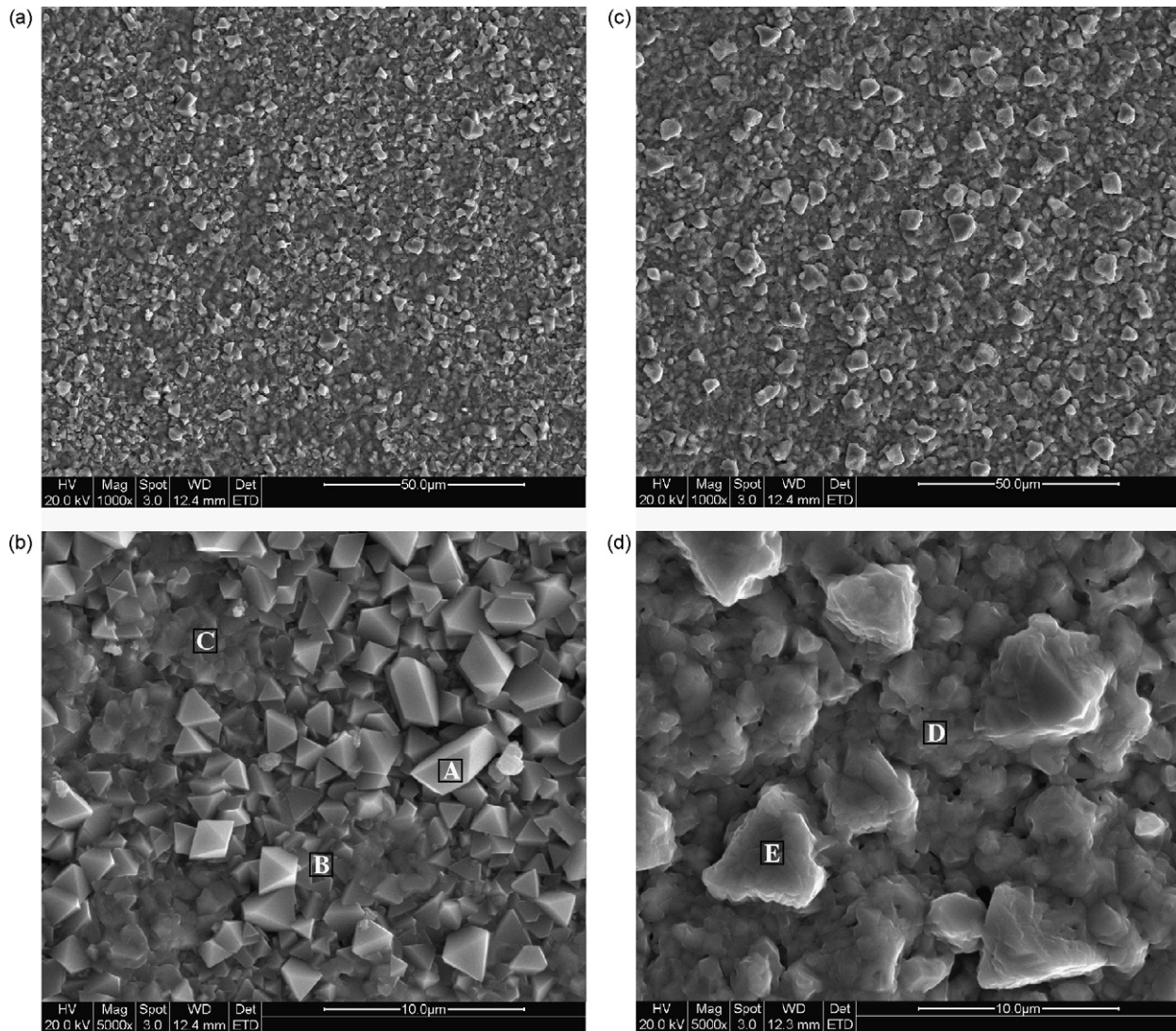
clusters with higher Cr content are probably the exposed Cr_2O_3. After 1000 h oxidation, the surface morphology of the oxide scale is dramatically changed with larger round-angular nodules (location E in Fig. 4d) uniformly distributed on dense oxide matrix (location D in Fig. 4d). As also shown in Table 2, the oxide matrix is determined as the Mn–Cr spinel and the round-angular nodules with higher Mn content are considered as Mn_2O_3. Fig. 5 shows the SEM secondary electron images of the surface oxide cyclically formed at 750 °C in air for 1000 h. Unlike the situation in the isothermal oxidation, the surface of cyclically grown oxide scale is more homogeneous and compact. As confirmed by EDS analysis at locations F and G in Fig. 5b (shown in Table 2), the surface oxide is rich in Mn and is probably Mn_2O_3. According to both EDS and XRD results, it may be expected that cyclic oxidation can significantly accelerate the outward diffusion of Mn ions, resulting in a complete Mn_2O_3 layer on top of the oxide scale. As also shown in Table 2, the oxide scale formed upon cyclic or isothermal exposure to air at 750 °C contain some Ti, especially in Cr_2O_3. Ti ion has a high mobility in Cr_2O_3 [20,24], which makes it possible to migrate from the substrate into the oxide scale and be dissolved in Cr_2O_3, partially substituting for Cr. Like Mn, the dissolved Ti may also expand the lattice parameters of Cr_2O_3, resulting in its diffraction peak shifting to lower angles as shown in Fig. 2.

Fig. 6 presents the SEM back-scattering electron image of the cross-sectioned Fe–Cr alloy isothermally oxidized at 750 °C in air for 1000 h (Fig. 6a) and the corresponding EDS line scan profile (Fig. 6b) showing the element distribution across the oxide scale. A dense oxide scale is observed on the surface of the alloy with oxide nodules located on top of the oxide matrix. TiO_2 existed as an internal oxide is distributed along the grain boundaries of the alloy or sporadically inside the alloy substrate near the substrate/oxide scale interface. A Cr-rich oxide layer, identified as Cr_2O_3, is located adjacent to the alloy substrate; and the outer layer that is rich in Mn and Cr is the spinel matrix with the Mn-rich nodules Mn_2O_3 on top of it. In addition, Ti and Mn are found to be concentrated in the layer of Cr_2O_3, which confirms the expectation that Mn and Ti are partially dissolved in Cr_2O_3 and is supportive to the above discussion on EDS results (Table 2). The microstructure of the cross-sectioned oxide scale formed upon the cyclic oxidation at 750 °C in air for 1000 h and the corresponding EDS line profile are shown in Fig. 7a and b, respectively. The oxide morphology and the element distribution across the scale are similar to those of the oxide scale formed upon the isothermal oxidation, with an inner Cr-rich layer and an outer Mn-rich layer. However, in the case of cyclic oxidation, the oxide scale is somewhat thinner and more compact and well adhered to the substrate; a well developed outmost Mn_2O_3 layer is observed with a Mn–Cr spinel layer underneath and a Cr_2O_3 layer adjacent to the substrate.

Previous studies [3,17] indicated that the oxidation process of Fe–Cr alloys with some Mn element is controlled by outward diffusion of cations through the well-developed Cr_2O_3 layer. Mn ions diffuse faster than Cr ions in Cr_2O_3, resulting in a double-layered oxide scale with Mn–Cr spinel on top of Cr_2O_3. In the present alloy, the outward diffusion of Cr and Mn at the initial stage of oxidation (200 h) mainly formed Cr_2O_3 and Mn–Cr spinel double layer structure as that happened in conventional Fe–Cr-based stainless steels, which is confirmed by XRD (Fig. 3) and EDS (Fig. 4b). However, the difference between this alloy and conventional Fe–Cr stainless steels is that this alloy contains higher content of Mn (1.05 wt.%), further outward diffusion of excessive Mn in subsequent oxidation leads to the formation of Mn_2O_3 on the surface of the oxide scale, whereas the Cr_2O_3 and Mn–Cr spinel underneath continuously grow. From thermodynamic point of view, the partial oxygen pressure for forming Mn_2O_3 is the highest among the oxides in the scale, which dictates that Mn_2O_3 only can exist in the outmost layer where has full exposed to the air. It is also expected that a full layer

Table 2
The EDS analysis results from locations A to G shown in b.

Area	Mn (at.%)	Cr (at.%)	O (at.%)	Ti (at.%)	Fe (at.%)
A	28.39	29.00	36.22	0.75	5.64
B	23.75	26.09	42.71	1.39	6.06
C	12.06	33.98	39.29	3.32	11.35
D	23.23	28.35	43.82	3.78	0.83
E	40.38	14.65	43.47	0.92	0.58
F	35.29	8.62	55.32	0.77	–
G	35.55	9.54	54.09	0.82	–

Fig. 4. SEM secondary electron images showing the surface morphology of the oxide scale of the Fe–Cr alloy isothermally oxidized at 750 °C in air for 200 h (a and b) and 1000 h (c and d).

of Mn_2O_3 will be established for longer time oxidation, no matter the alloy is isothermally or cyclically oxidized, which will effectively inhibits the outward diffusion of Cr to form Cr-containing species on top of the scale and suppresses the Cr evaporation. At current stage, it still remains puzzled over the effect of thermal cycle on accelerating Mn outward diffusion and improving the adherence of the scale to the substrate.

3.2. Oxidation kinetics

The oxidation resistance of an alloy is usually characterized by its oxidation kinetics. Fig. 8 shows the oxidation kinetics of the presently developed Fe–Cr alloy in both isothermal and cyclic oxidization modes at 750 °C in air for up to 1000 h. The curves were plotted as the square of specific area weight gain against the oxidation time, so that the oxidation kinetics can be explicitly presented. As expected, in both the cases, the square of specific area weight gain caused by oxidation increases linearly with the oxidation time, satisfying the diffusion-controlled parabolic kinetics law as follows:

$$\left(\frac{\Delta W}{A}\right)^2 = Kt \tag{2}$$

where ΔW is the weight gain of the sample, A is the surface area of the sample, t is the oxidation time, and K ($g^2 \, cm^{-4} \, s^{-1}$) is the parabolic rate constant. The slope of the straight line in Fig. 8 represents the parabolic rate constant K, i.e. oxidation rate. The experimentally obtained K for the Fe–Cr alloy isothermally oxidized at 750 °C in air is $6.4 \times 10^{-14} \, g^2 \, cm^{-4} \, s^{-1}$ with no obvious oxidation rate change during 1000 h of exposure. However, in the case of the cyclic oxidation, the Fe–Cr alloy experienced an initial stage of fast oxidation (0–150 h) with a rate constant of $7.6 \times 10^{-14} \, g^2 \, cm^{-4} \, s^{-1}$, followed by a slower steady oxidation (150–1000 h) at a rate of $5.1 \times 10^{-14} \, g^2 \, cm^{-4} \, s^{-1}$ which is slightly lower than that obtained in the isothermal oxidation. The transition in oxidation rate occurred in the cyclic oxidation is believed to be caused by the formation of a continuous and compact Mn_2O_3 layer. The well-developed Mn_2O_3 layer which covered the whole surface is expected to inhibit both the outward diffusion of cations (such as Cr) and inward diffusion of anions (such as O), and consequently reduce the scale growth rate. The total oxidation weight gain after 1000 h exposure to air at 750 °C is 0.47 and 0.44 mg cm^{-2} for the isothermal and the cyclic oxidations, respectively. Thermal cycle seems to have a positive effect on reducing the oxidation rate. This behavior is preferred for SOFC interconnect application; however, the reason behind this phenomenon still needs to be understood.

(a)

(b)
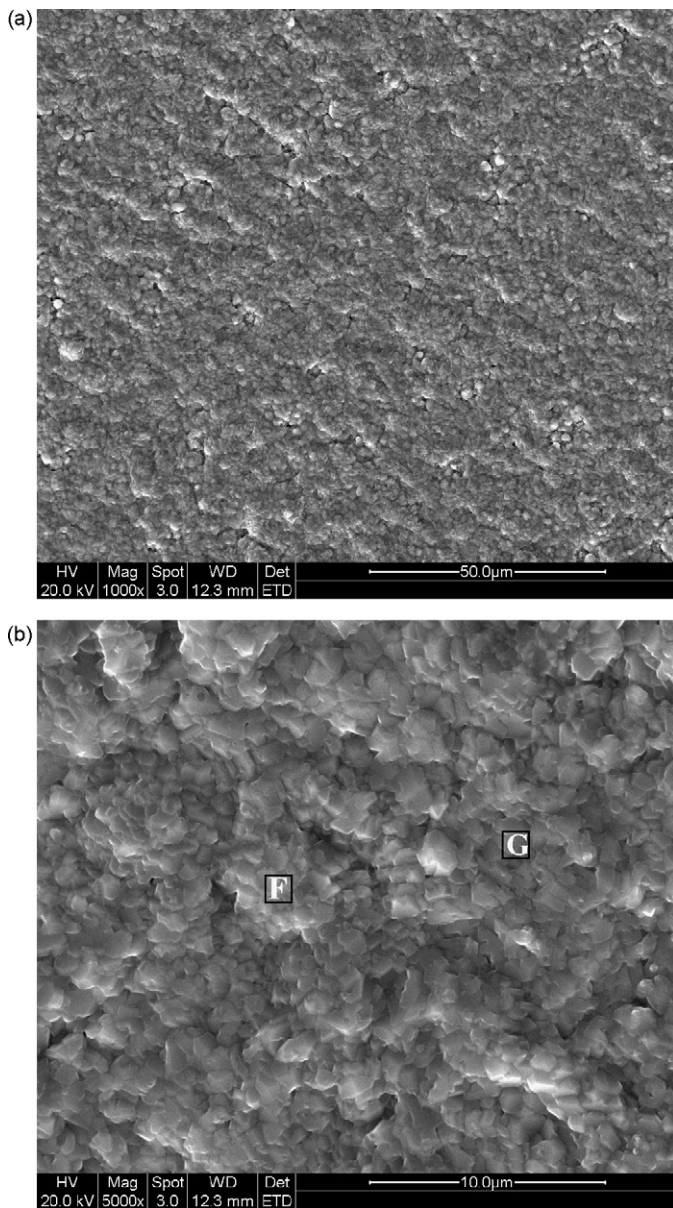
Fig. 5. SEM secondary electron images showing the surface morphology of the oxide scale of the Fe–Cr alloy cyclically oxidized at 750 °C in air for 1000 h: (a) 1000× and (b) 5000×.

3.3. Electrical property of the oxide scale

One of the key requirements for metallic interconnect materials is low and stable electrical resistance during SOFC operation. The ASR, which reflects both the electrical conductivity and thickness of the oxide scale, is usually adopted for characterizing the electrical property of the oxide scale. The electrical resistance of the substrate alloy is negligible as it is insignificant compared with the formed oxide scale, and the main contribution of the metallic interconnect to the ASR comes from the oxide scale. Fig. 9 shows the measured ASR of the Fe–Cr alloy pre-oxidized at 750 °C in air isothermally for various hours or cyclically for 1000 h as a function of measurement temperature. The measured ASR increases with decreasing measurement temperature, and log(ASR/T) is linearly proportional to 1/T, showing the electrical characteristic of semi-conductors described by the Arrhenius equation:

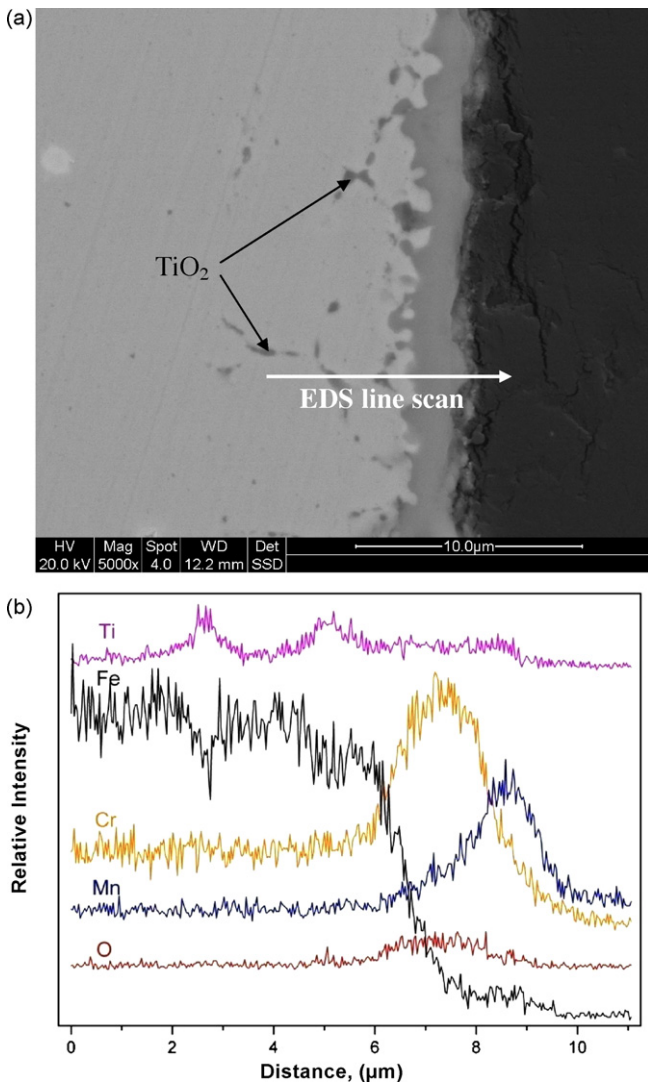$$\frac{\text{ASR}}{T} = A\exp\left(\frac{E_a}{kT}\right) \tag{3}$$

(a)

(b)
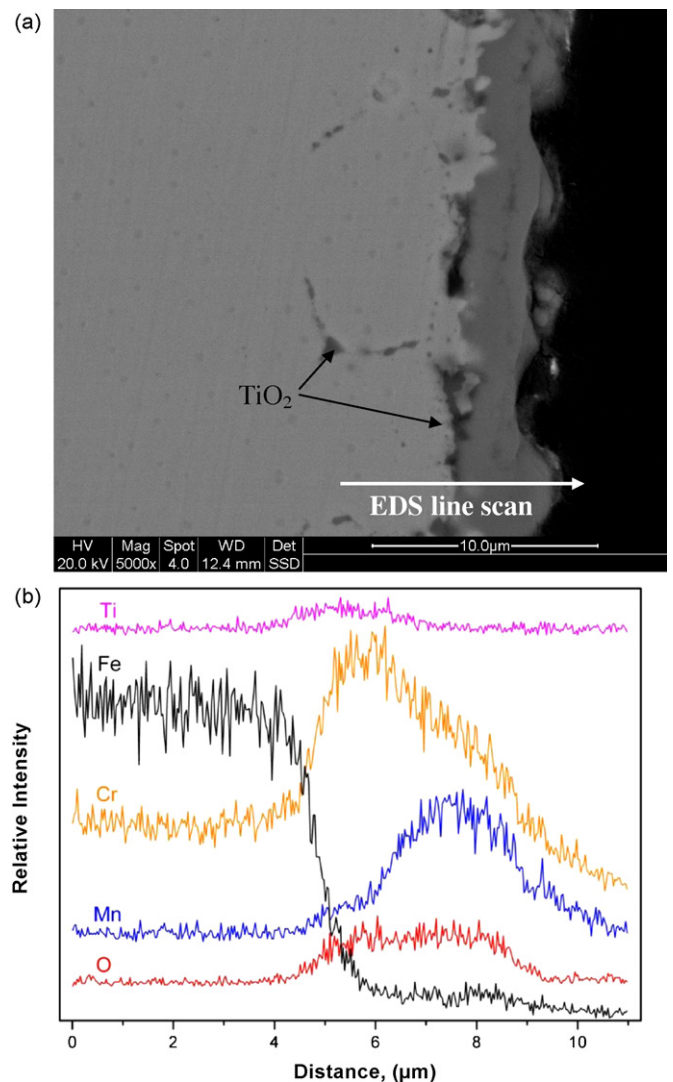
Fig. 6. SEM backscattering electron morphology (a) and EDS line scan profile (b) of the cross-sectioned Fe–Cr alloy isothermally oxidized at 750 °C in air for 1000 h.

where A is a pre-exponential constant, T is the absolute temperature, E_a is the activation energy for the movement of charge carriers, and k is the Boltzmann's constant. The calculated E_a from the dependence of ASR on temperature shown in Fig. 9 is around 0.27 eV, which is close to that of the doped Cr_2O_3 [25]. This suggests that the Cr_2O_3 which possesses the highest resistivity controls the electrical property of the formed oxide scale. The ASR increases with the isothermal oxidation time for all measuring temperatures, corresponding to the continuous growth of the oxide scale. At 750 °C, thermal cycle slightly reduces the ASR from 11 mΩ cm² for isothermal oxidation at 750 °C in air for 1000 h to 9.9 mΩ cm². Such ASR values are lower than that of the conventional Fe–Cr alloys and comparable with that of some Ni-based alloys [22,26].

The ASR can also be expressed as a combination of the thickness (l) and the electrical resistivity (ρ) of the oxide scale:

$$\text{ASR} = \rho l \tag{4}$$

According to Eq. (2), the square of the oxide scale thickness should be proportional to the oxidation time. Assuming the resistivity of the oxide scale is somewhat unchanged with oxidation time, then it can be approximately extrapolated that the ASR value of the alloy after 40,000 h of oxidation at 750 °C in air will be in the range of 63–68 mΩ cm². This estimated ASR value is significantly lower
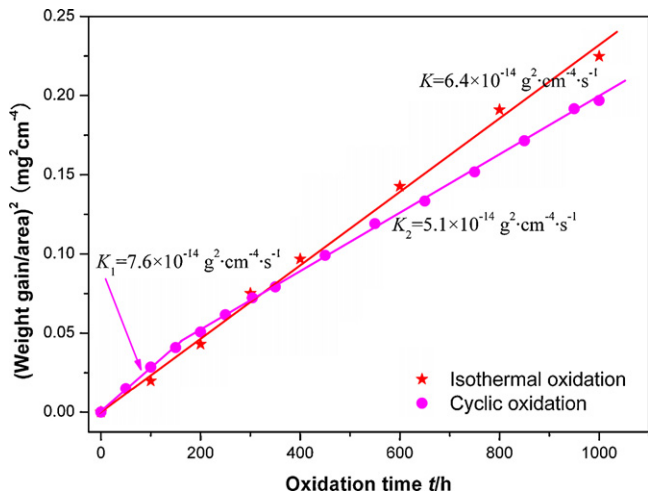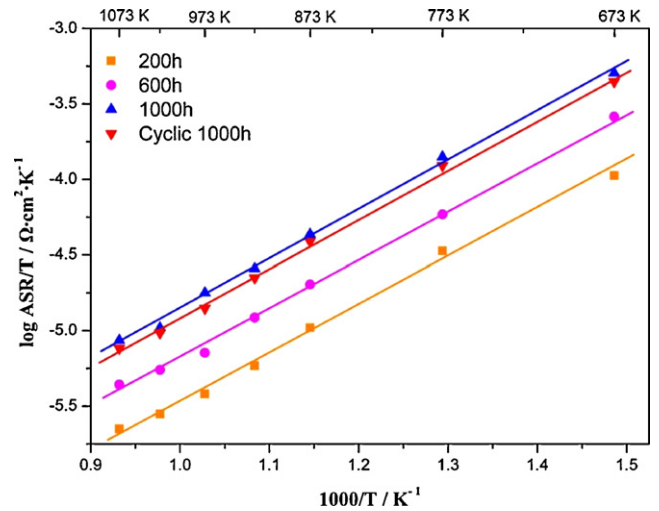
Fig. 9. ASR of the Fe–Cr alloy pre-oxidized at 750 °C in air for various hours as a function of measurement temperature.

than the conventionally required $100 \, m\Omega \, cm^2$ for metallic interconnect materials. Among the oxides formed in the scale, Cr_2O_3 has the highest resistivity. Such low ASR value is attributed to the improved oxidation resistance, the formation of highly conductive Mn_2O_3 [22] and Ti doping in Cr_2O_3 [21,27].

4. Conclusions

Based on this study, the following conclusions can be reached:

(1) The thermally grown oxide scale of the developed Fe–Cr alloy after either isothermal or cyclic oxidation at 750 °C in air for up to 1000 h mainly consists of Cr_2O_3, Mn–Cr spinel and Mn_2O_3, presenting a multi-layered structure with Mn–Cr spinel in-between the underneath Cr_2O_3 and the top Mn_2O_3. Mn_2O_3 nodules form on the surface of the scale initially and gradually cover the whole area densely with oxidation time prolonged. TiO_2 internal oxide is also formed sporadically in the alloy underlying the scale and along the grain boundaries.

(2) High mobility of Ti and Mn ions in oxides promotes their outward diffusion into the formed oxide scale, resulting in doped Cr_2O_3 and spinel with shifted XRD diffraction peaks to the low angles. In the meantime, the lattice parameters of the alloy substrate underneath the oxide scale gradually shrink as the continuous outward diffusion of cations (Cr, Mn, Ti), leading to a depletion of alloying element in the area and peak shift of XRD diffraction to the higher angles.

(3) The oxidation kinetics obtained at 750 °C in air under both isothermal and cyclic oxidation conditions obeys the parabolic law with a rate constant in the range of 5.1×10^{-14} to $7.6 \times 10^{-14} \, g^2 \, cm^{-4} \, s^{-1}$. In the case of cyclic oxidation, the rate constant is decreased after 150 h oxidation due to the formation of densely packed Mn_2O_3 on top of the scale.

(4) The ASR value, measured at 750 °C in air, of the alloy pre-oxidized isothermally or cyclically at 750 °C in air for up to 1000 h is around $10 \, m\Omega \, cm^2$. The attractive electrical property of the oxidized Fe–Cr alloy can be attributed to its excellent oxidation resistance and the formation of doped Cr_2O_3, spinel and highly conductive Mn_2O_3.

(5) The developed alloy has an excellent cyclic oxidation resistance, demonstrating improved oxide scale adherence, enhanced formation of densely packed Mn_2O_3 and lowered ASR. The mechanism behind these phenomena needs to be further understood.

Fig. 7. SEM backscattering electron morphology (a) and EDS line scan profile (b) of the cross-sectioned Fe–Cr alloy cyclically oxidized at 750 °C in air for 1000 h.

Fig. 8. Oxidation kinetics of the Fe–Cr alloy oxidized at 750 °C in air for 1000 h.

Acknowledgements

References

[1] W.Z. Zhu, S.C. Deevi, Mater. Sci. Eng. A348 (2003) 227–243.
[2] J.W. Fergus, Mater. Sci. Eng. A397 (2005) 271–283.
[3] J. Pu, J. Li, B. Hua, G. Xie, J. Power Sources 158 (2006) 354–360.
[4] T. Horita, H. Kishimoto, K. Yamaji, Y. Xiong, N. Sakai, M.E. Brito, H. Yokokawa, J. Electrochem. Soc. 153 (2006) A2007–A2012.
[5] J. Rufner, P. Gannon, P. White, M. Deibert, S. Teintze, R. Smith, H. Chen, Int. J. Hydrogen Energ. 33 (2008) 1392–1398.
[6] L. Cooper, S. Benhaddad, A. Wood, D.G. Ivey, J. Power Sources 184 (2008) 220–228.
[7] J. Froitzheim, G.H. Meier, L. Niewolak, P.J. Ennis, H. Hattendorf, L. Singheiser, W.J. Quadakkers, J. Power Sources 178 (2009) 163–173.
[8] S.P. Jiang, S. Zhang, Y.D. Zhen, J. Mater. Res. 20 (2005) 747–758.
[9] S.P. Jiang, Y.D. Zhen, S. Zhang, J. Electrochem. Soc. 153 (2006) A1511– A1517.
[10] M. Stanislowski, E. Wessel, K. Hilpert, T. Markus, L. Singheiser, J. Electrochem. Soc. 154 (2007) A295–A306.
[11] T. Horita, Y. Xiong, K. Yamaji, N. Sakai, H. Yokokawa, J. Electrochem. Soc. 150 (2003) A243–A248.
[12] Z. Yang, M.S. Walker, P. Singh, J.W. Stevenson, T. Norby, J. Electrochem. Soc. 151 (2004) B669–B678.
[13] B. Hua, J. Pu, W. Gong, J. Zhang, F. Lu, J. Li, J. Power Sources 185 (2008) 419–422.
[14] H. Kurokawa, C.P. Jacobson, L.C. DeJonghe, S.J. Visco, Solid State Ionics 178 (2007) 287–296.
[15] W. Qu, J. Li, D.G. Ivey, J. Power Sources 138 (2004) 162–173.
[16] W. Qu, J. Li, D.G. Ivey, J.M. Hill, J. Power Sources 157 (2006) 335–350.
[17] Z. Yang, J.S. Hardy, M.S. Walker, G. Xia, S.P. Simner, J.W. Stevenson, J. Electrochem. Soc. 151 (2004) A1825–A1831.
[18] D.E. Alman, P.D. Jablonski, Int. J. Hydrogen Energ. 32 (2007) 3743–3753.
[19] Z. Yang, G. Xia, X. Li, J.W. Stevenson, Int. J. Hydrogen Energ. 32 (2007) 3648–3654.
[20] F. Abe, H. Araki, H. Yoshida, M. Okaka, Oxid. Met. 27 (1987) 21–36.
[21] H. Nagai, K. Ohbayashi, J. Am. Ceram. Soc. 72 (1989) 400–403.
[22] S.J. Geng, J.H. Zhu, J. Power Sources 160 (2006) 1009–1016.
[23] Z. Lu, J. Zhu, E.A. Payzant, M.P. Paranthaman, J. Am. Ceram. Soc. 88 (2005) 1050–1053.
[24] S. Taniguchi, N. Hongawara, T. Shibata, Mater. Sci. Eng. A307 (2001) 107–112.
[25] A. Holt, P. Kofstad, Solid State Ionics 69 (1994) 137–143.
[26] S.J. Geng, J.H. Zhu, Z.G. Lu, Solid State Ionics 177 (2006) 559–568.
[27] A. Atkinson, M.R. Levy, S. Roche, R.A. Rukin, Solid State Ionics 177 (2006) 1767–1770.